A new approach for predicting the pool boiling heat transfer coefficient of refrigerant R141b and its mixtures with surfactant and nanoparticles using experimental data

O. Khliyeva[1] · V. Zhelezny[1] · T. Lukianova[1] · N. Lukianov[1,2] · Yu. Semenyuk[1] · A. L. N. Moreira[3] · S. M. S. Murshed[3] · Elena Palomo del Barrio[4,5] · A. Nikulin[4]

Abstract

In the present study, the pool boiling process for the refrigerant R141b and its mixtures with Span 80 surfactant and TiO_2 nanoparticles has been examined. The results for the heat transfer coefficient (HTC) were taken at various boiling pressures (0.2, 0.3, 0.4 MPa) in the range of the heat fluxes 5.8–56.4 kW m^{-2} and for the internal boiling characteristics (IBC) such as the bubble departure diameter, frequency and velocity of bubble growth at atmospheric pressure in the range of the heat fluxes 29.6–57.0 kW m^{-2}. We found that the additives of Span 80 and Span 80/TiO_2 nanoparticles enhance the HTC at the lower heat flux densities and pressures. However, at higher values of the heat flux and pressure the HTC was deteriorated by the additives. At the same time, no significant impact was obtained for the IBCs. An analysis of the Rensselaer Polytechnic Institute model performance for the case when experimental data on the nucleation sites density is unavailable has revealed no qualitative agreement between experimental and predicted data on the HTC. Thus, we proposed a new approach that combines limited set of the experimental data (LSED) with correlations of the IBC's versus heat flux and pressure. Finally, the LSED allowed to achieve both qualitative and quantitative agreement (within ± 10%) between predicted and experimental data on the HTC.

Keywords Pool boiling · Heat transfer coefficient · Experiment · Model · Surfactant · Nanoparticles · Nanofluid

List of symbols

A, B, C Empirical coefficients
A Surface area of the heater (m^2)
$\bar{d}_b$ Mean bubble departure diameter (mm)

d_h Diameter of heating surface (m)
$\bar{f}_b$ Mean bubble departure frequency (s^{-1})
h Heat transfer coefficient (kW m^{-2} K^{-1})
k Thermal conductivity (W m^{-1} K^{-1})
n_b Nucleation site density (m^{-2})
P Pressure (MPa)
q Heat flux density (kW m^{-2})
Q Heat flux (kW)
r_{mean} Mean equivalent radius of nanoparticles in nanofluid (nm)
R_{rc} Resistance of resistance coil (Ω)
T Temperature (K)
U_h Voltage drop across the heater (V)
U_{rc} Voltage drop across the resistance coil (V)
$\bar{w}_b$ Mean velocity of bubble growth (mm s^{-1})

Greek symbols

Δh Heat of vaporization (J kg^{-1})
ΔT Wall superheat, $T_S - T_w$ (K)
π Reduced pressure, P/P_C
ρ Density (kg m^{-3})

✉ A. Nikulin
anikulin@cicenergigune.com

1   Institute of Refrigeration, Cryotechnologies and Ecoenergetics, Odessa National Academy of Food Technologies, 1/3 Dvoryanskaya Str., Odessa 65082, Ukraine

2   Institute of Thermomechanics of the CAS, v. v. i., Dolejškova 1402/5, 18200 Prague, Czech Republic

3   Center for Innovation, Technology and Policy Research, IN+, Instituto Superior Técnico, Universidade de Lisboa, Av. Rovisco Pais 1, 1049-001 Lisbon, Portugal

4   Centre for Cooperative Research on Alternative Energies (CIC energiGUNE), Basque Research and Technology Alliance (BRTA), Alava Technology Park, Albert Einstein 48, 01510 Vitoria-Gasteiz, Spain

5   Ikerbasque – Basque Foundation for Science, María Díaz Haroko 3, 48013 Bilbao, Spain

σ	Surface tension (N m^{-1})
τ	Time (h)

Subscripts

1.1	Thermophysical properties at $P_{0.1} = 0.1013$ MPa
C	Property under critical conditions
S	Property under saturated conditions
w	Property at wall (heating surface) temperature

Superscripts

calc	Calculated value
exp	Experimental value
′	Liquid phase
″	Vapor phase

Abbreviations

CTAB	Cetyltrimethylammonium bromide
EDX	Energy-dispersive X-ray analysis
HTC	Heat transfer coefficient
IBC	Internal boiling characteristics
LSED	Limited set of experimental data
RMSE	Root mean square error
SEM	Scanning electron microscopy
SDBS	Dodecylbenzenesulfonic acid sodium salt
SDS	Dodecyl sulfate sodium salt
ST	Spectral turbidity
TEM	Transmission electron microscopy

Introduction

The accurate information on the heat transfer coefficient (HTC) is crucial for the optimal design of energy equipment in which the pool boiling is utilized. To date, many approaches have been proposed to predict the HTC under pool boiling conditions. The simplest ones are the correlations in the form of equations $h \sim q^c$, $h \sim \Delta T^c$ or $q \sim \Delta T^c$, where h, q and ΔT represent, respectively, the HTC, the heat flux density supplied by the heating element and the difference between the temperature at the surface of the heating element and the saturation temperature of the boiling liquid. The exponent C and pre-factors are determined by fitting experimental data to the equations above [1]. These correlations usually provide quite good agreement between calculated HTC values and measurements. However, their use is very restricted. They can only be applied within the experimental framework used to establish them. To partially overcome such limitation, different semiempirical correlations have been proposed. These correlations can be arranged in ascending order of volume of initially required information:

- Correlations utilizing the effect of the pressure on the pool boiling [2–5]. Besides pressure, the correlations may require information on the roughness of the boiling surface [3–5];
- Correlations utilizing thermophysical properties of the liquid [6, 7]. Such correlations may also require specific constants to consider the liquid-surface combination [6];
- Correlations that combine both effects of the pressure and thermophysical properties on the boiling process [8];
- Correlations that combine effects of the thermophysical properties and some of the internal boiling characteristics (IBC), such as the bubble departure diameter and frequency [9, 10];
- Mechanistic models, such as the Rensselaer Polytechnic Institute (RPI), which consider all the IBC [11, 12].

It is worth to mention that establishing such correlations requires considerable experimental effort. Indeed, a large amount of experiments, covering a wide range of operating conditions, is needed for subsequent adjustments to be meaningful and reliable. Usually, the proposed correlations exhibit deviations from experimental data on the order of $\pm 20\%$ [5, 8]. Nevertheless, the deviations between models may come up to 150% [13]. Thus, semiempirical correlations do not guaranty required accuracy for system design and optimization. From the other hand, mechanistic models such as RPI may predict the boiling HTC more accurately [12, 13], but the model requires knowledge of the IBC that are unknown at the stage of energy system design.

Considering the aforementioned issues, we can formulate the aim of the present study as a test for a new approach to the pool boiling HTC prediction for the pure liquids and their mixtures with surfactant and nanoparticles using limited set of the experimental data (LSED) and RPI model.

We believe that the proposed approach is a rational compromise between theoretical prediction of the HTC (that usually gives high uncertainty) and experimental investigation of the HTC that is expensive and may take a long time.

Experimental

Materials: Preparation of nanofluid and its stability

The following materials have been used in the experiments: refrigerant R141b (CAS No. 1717-00-6, supplied by Zhejiang MR Refrigerant Co. Ltd, China, 0.998 (kg kg^{-1}) pure; TiO$_2$ nanoparticles (CAS No. 1317-70-0) and Span 80 surfactant (CAS No. 1338-43-8) both supplied by Sigma-Aldrich with a purity 0.999 (kg kg^{-1}). The data obtained from SEM microscopy have revealed that the nanoparticles exist in the form of the clusters in the powder. There are no impurities detected by EDX (see Fig. 1a, c). As stated by supplier, the size of nanoparticles does not exceed 25 nm and this statement was confirmed by TEM microscopy. As can

Fig. 1 TiO$_2$ nanoparticles: **a** SEM image, **b** TEM image and **c** EDX spectrum

(a)

(b)

(c)
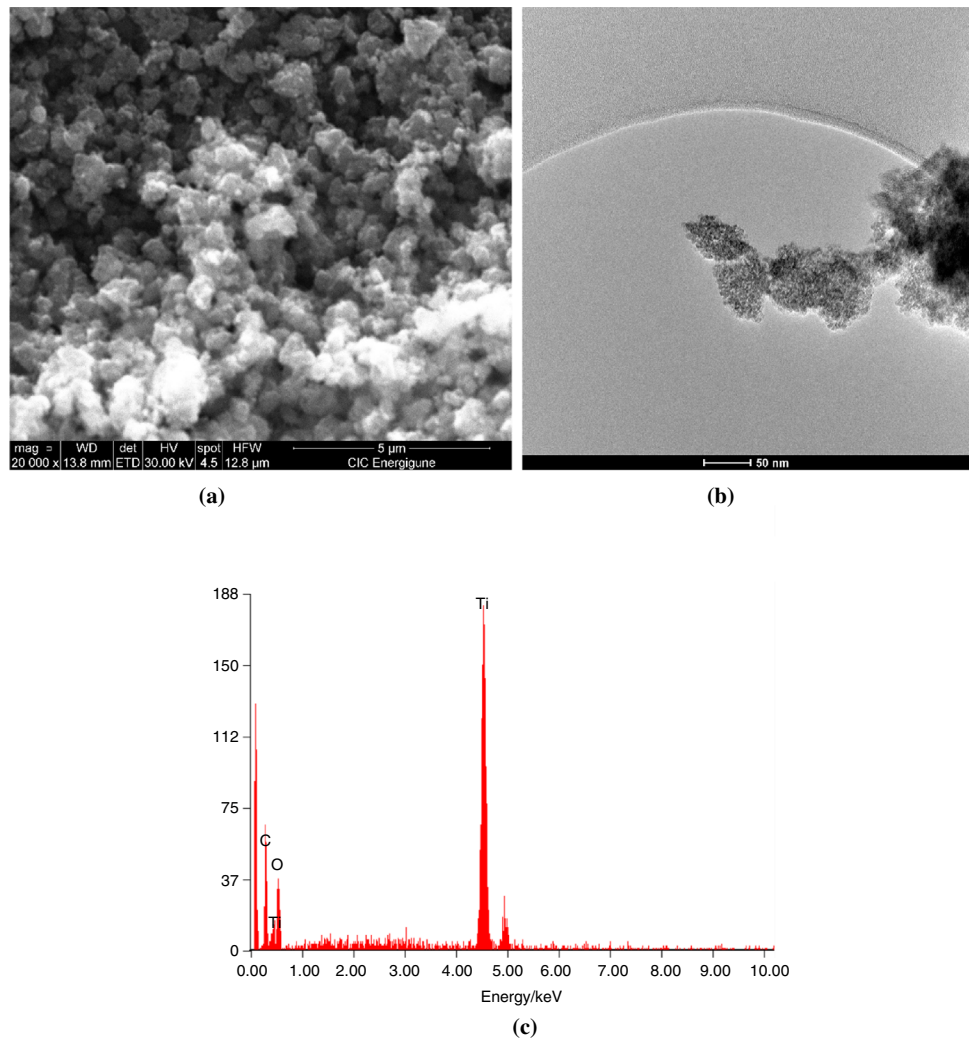
be seen from Fig. 1b, the size of the majority of individual nanoparticles is less than 15 nm.

The choice of nanoparticle material (TiO$_2$) was driven by their chemical stability, proven technology of production and low cost. Refrigerant R141b was selected as the working fluid for several reasons: (1) R141b exists in a liquid state under ambient conditions; thus, it is convenient to use R141b as a base liquid for the nanofluid preparation and to carry out boiling experiments; (2) despite the differences in physical properties of R141b and commonly used today refrigerants such as R134a and R410A, all of them belong to the same group of halogenated hydrocarbons. Therefore, the obtained results on the boiling performance of the "model" system R141b/nanoparticles are expected to be qualitatively similar to all hydrofluorocarbon refrigerants; (3) most of the reported studies on the

pool boiling process for the refrigerant-based nanofluids were performed with R141b. It is evident that the use of the identical thermodynamic systems is advisable for subsequent comparison of experimental data obtained by different researchers.

The two-step method was applied to prepare the nanofluids. The method consists of the following stages:

1. Sonication of the mixture of nanoparticles and surfactant in the refrigerant during 30 min using ultrasound bath Codison CD 4800 (frequency 42 kHz, power 0.07 kW);
2. Ball milling by 2 mm in diameter ZrO$_2$ balls during 12 h;
3. One more cycle of sonication (see first step).

As can be seen from Fig. 2, it was not possible to create stable nanofluid without surfactant additives. The obtained results contradict to the findings reported in [14], where stability of the R141b/TiO$_2$ nanofluid was achieved without surfactant. We conducted additional studies in order to select proper surfactant and its concentration to ensure the stability of nanofluid. Several surfactants were used: anionic SDBS (CAS No. 25155-30-0) and SDS (CAS No. 151-21-3), cationic CTAB (CAS No. 57-09-0) and nonionic Span 80 (CAS No.1338-43-8) (all supplied by Sigma-Aldrich). During surfactant selection, all nanofluid samples were prepared by the method described above with only one difference—the surfactants were introduced to the nanofluid at the third step. It was found that colloidally stable nanofluid was prepared only when we used the nonionic surfactant Span 80. Thereafter, the selection of the optimal concentration has been performed. Prepared sample of the nanofluid in comparison with the pure R141b that placed inside of the hermetic optical cell is shown in Fig. 3.

The spectral turbidity (ST) method [15–18] was applied to study of the colloidal stability of nanofluids by measuring the mean nanoparticles radius. The previous results obtained for the average size of Al$_2$O$_3$ nanoparticles in isopropanol [18] have confirmed good agreement between the ST and dynamic light scattering methods (DLS). The ST method was performed using the spectrophotometer Shimadzu UV-120-02. For the period of measurements, the samples of nanofluid were placed in open optical cells with the optical path of 1.05 mm.

The radius of the nanoparticles was measured several times over 2 months: immediately after nanofluid preparation, during boiling experiment [sampling was carried out directly from the experimental setup (see Sect. 2.2)], after the end of experiment for the nanofluid that was stored in a sealed test tube. Before sampling, the nanofluid was
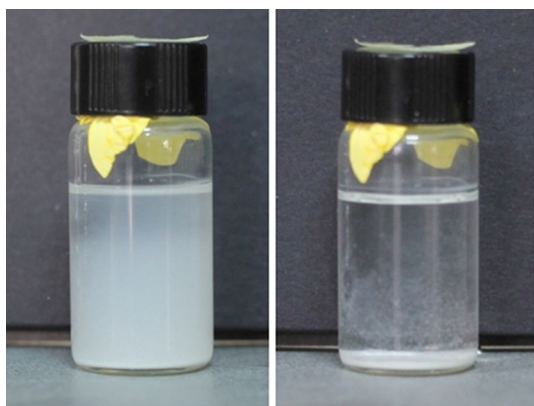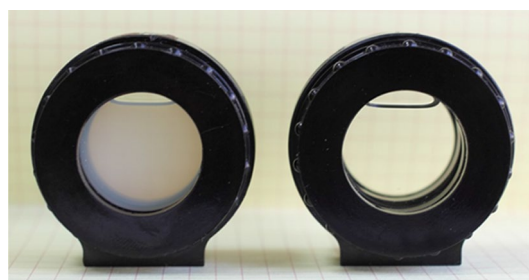

Fig. 3 Snapshot of the nanofluid R141b/Span 80/TiO$_2$ (99.80/0.10/0.10 mass%, 1 h after preparation) in comparison with pure R141b

intensively mixed. The results of nanoparticles radius measurements are shown in Fig. 4.

The results of ST studies show that after preparation of nanofluid, the mean equivalent radius of the nanoparticles is about 104 nm. After several days of boiling experiments, it grows up to 125 nm. Any further increase in the size of nanoparticles over time was not observed. Higher scattering of the values of the nanoparticles radius measured during boiling process (blue cycles in Fig. 4) is probably gathered with local change in the nanoparticles size distribution as a result of the heat and mass transfer processes.

Experimental setup for HTC study

A cylindrical (diameter—70 mm, volume—1 dm^3) measuring cell, equipped with side plane parallel quartz windows, served as a boiler. Stainless steel (AISI 321) capillary bent to M-shape having 2 mm outside diameter and 0.1 mm wall thickness forms the heating surface. The length of the heater
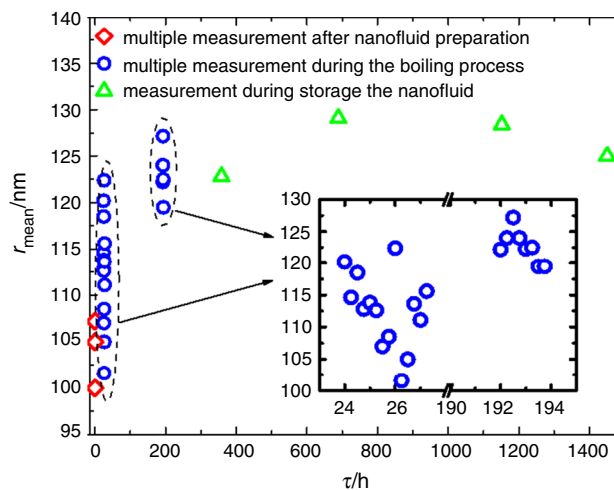

Fig. 2 Snapshots of the nanofluid R141b/TiO$_2$ (99.90/0.10 mass%) without surfactant: (left) 1 h after preparation and (right) 18 h after preparation

Fig. 4 Nanoparticles mean equivalent radius r_{mean} versus time τ determined by the ST method for the nanofluid R141b/Span 80/TiO$_2$ (99.80/0.10/0.10 mass. %) (Note: green triangles represent each measurement taken with large time interval)

is 748 mm. The heat flux was generated by Joule effect using high-power electrical supply.

Electric power supplied to the heater was determined by the compensation method using 0.001 Ohm reference resistance coil (P322). An average surface temperature of the heater was measured by resistance thermometer which is made of platinum wire with 0.1 mm in diameter and stretched out across the capillary. The resistance of platinum wire was also determined by the compensation method using 10 Ohm reference resistance coil (P321). The compensation method was used with the aim to minimize the uncertainty of those parameters. The boiling temperature was measured by copper resistance thermometer. The saturated vapor pressure of the samples in the boiler was measured by a pressure transducer WIKA A-10. Finally, all measurements of electrical parameters were taken with digital multimeter PICOTEST M3511A.

Heat flux Q was calculated using the following equation

$$Q = \frac{U_h U_{rc}}{R_{rc}} \qquad (1)$$

where U_h and U_{rc} are the voltage drops across the heater and resistance coil, respectively, V; R_{rc} is resistance of resistance coil, Ohm.

Heat transfer coefficient h was calculated by the following equation

$$h = \frac{Q}{A \Delta T} \qquad (2)$$

where A is the surface area of the heater, m²; ΔT is temperature difference between reading of the resistance thermometer inside the heater and copper resistance thermometer, K.

More details on the experimental setup and procedure, as well as the pool boiling test results, were described elsewhere [13]. More specifically, main parts of the boiler used in this study could be found in [19].

Since the optical density of the R141b/Span 80/TiO$_2$ nanofluid is high and the optical path between the sight glasses provided in this experimental setup is long (90 mm)
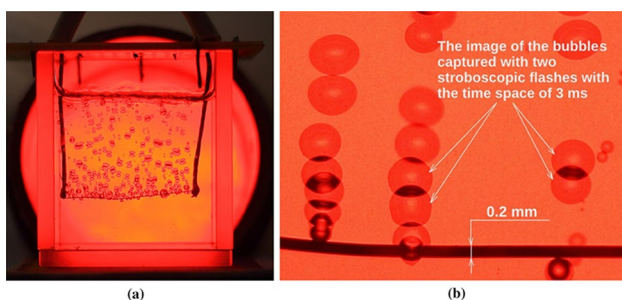

Fig. 5 Snapshots: **a** experimental cell for the IBC study, **b** boiling process for R141b/Span 80 at 29.6 kW m⁻² (resolution 150 pixels per 1 mm)

[13, 19], it was not possible to use it to obtain information on the IBCs by the method that will be described below.

Experimental setup for IBC study

In order to obtain the information on the IBC at the atmospheric pressure, an open optical cell with the optical path 30 mm was used (see Fig. 5a). A Ni–Cr wire 0.2 mm in diameter and 86 mm in length served as a test section. Power supply BVP (30 V/50 A) with power stabilization accuracy 0.01 W was used to generate the heat flux. The snapshots of boiling process have been taken with help of the camera (Canon EOS 1100D) and the stroboscope. A set of ten light emitting diodes (LED) (1 W) having peak wavelength at 650 nm were utilized as a light source in the stroboscope. Those LEDs were chosen because the maximum photosensitivity of image sensor installed in Canon EOS 1100D is near 650 nm wavelength. The optical cell for the IBC measurements, the light source and the camera were aligned along the same optical axis during the experiments.

As an example of the stroboscopic effect, the snapshot of boiling process for the R141b/Span 80 at the heat flux 29.6 kW m⁻² is shown in Fig. 5b. The stroboscope operated in a mode of 50 μs of the light pulse and 3 ms interval between pulses. We would like to emphasize that the application of the stroboscopic effect allows to get digital images of high-speed processes in high resolution (depending from characteristics of the digital camera) that is much higher comparing to high-speed cameras in the medium price range. Moreover, due to the stroboscopic effect it is possible to analyze the bubble departure frequency. However, the disadvantage of the stroboscope application is the overlapping images that complicate their subsequent processing.

The set of 100–160 bubbles was collected to determine the mean bubble departure diameter $\bar{d}_b$ and 70–120 bubbles to determine the mean bubble departure frequency $\bar{f}_b$.

Uncertainty analysis

The uncertainty analysis was carried out according to guidelines for evaluating and expressing the uncertainty [20]. Both components of uncertainty type A "random" and type B "systematic" have been considered. The combined standard uncertainty of the measurement results can be calculated as:

$$u_c^2(y) = \sum_{i=1}^{N} \left(\frac{df}{dx_i} \right)^2 u^2(x_i), \qquad (3)$$

where $\frac{df}{dx_i}$ is the sensitivity coefficient; $u(x_i)$ is the standard uncertainty associated with the input estimate x_i.

The evaluated maximum combined standard uncertainties (type B "systematic") are listed in Table 1. The limits of

the expanded uncertainty for the HTC including both types of uncertainty for the obtained experimental data are presented in Fig. 6a–c. For the experimental data on the bubble departure diameter and frequency, the expanded uncertainty $U = k u_c(y)$ can be estimated at coverage factor $k = 2$ for 0.95% level of confidence.

Experimental results

Besides the effect of nanoparticles presence, the effect of surfactant admixture on the boiling process has been analyzed [21, 22]. Thus, in the experiments we have examined the following working fluids:

- pure refrigerant R141b;
- R141b/Span80 solution (99.90/0.10 mass%) (shown as R141b/Surf. in the figures);
- nanofluid R141b/Span80/TiO$_2$ (99.80/0.10/0.10 mass%) (shown as R141b/Surf./TiO$_2$ in the figures).

HTC results

Experiments were performed using the experimental setup mentioned in Sect. 2.2 at several pressures (0.20, 0.30, 0.40 MPa) and corresponding boiling temperatures (52.9, 67.1, 77.9 °C) in the range of the heat fluxes 5.81–56.44 kW m^{-2}. The experimental results on the HTC are shown in Fig. 6a–c. As can be seen, the error bars become wider at the higher heat fluxes. This can be explained by the pulsating nature of the boiling process at the elevated heat fluxes that finally resulted in higher values of type A uncertainty. In order to analyze the effects of the surfactant and nanoparticles on the HTC, firstly, the experimental HTC data were fitted by the following equation

$$h = A \cdot q^{\mathrm{B}}, \tag{4}$$

where A and B are coefficients (listed in Table 2).

Thereafter, the relative deviations of the HTC between pure R141b and its mixtures with Span 80 and Span 80/TiO$_2$ were calculated (see Fig. 7a, b).

Similar influence of the surfactant Span-80 and Span-80/TiO$_2$ was found for the HTC of the R141b. Both admixtures lead to the higher HTC at the lower heat flux and pressures. This effect was mitigated with increasing the heat flux and, finally, the HTC became lower comparing to the pure R141b. Such dependence of the HTC may be beneficial for the plants that operate at the low heat fluxes and pressures simultaneously, for example, for the heat pumps and refrigerators.

Table 1 Results of uncertainty evaluation

Parameter	Maximum combined standard uncertainty
Mass fraction/kg kg^{-1}	2.5×10^{-5}
Heater surface area/m^2	7×10^{-6}
Heat flux Q/W	0.23
Wall temperature/K	0.07
Boiling temperature/K	0.06
Temperature difference/K	0.1
HTC/%	2
Bubble departure diameter/mm	0.04
Bubble departure frequency/s^{-1}	6

IBC results

The IBC (bubble departure diameter, bubble departure frequency and mean velocity of bubble growth) were studied experimentally under atmospheric pressure at three values of the heat fluxes (29.6, 42.2, 57.0 kW m^{-2}). Figure 8a–c depicts the pool boiling process at atmospheric pressure and heat flux equal to 57.0 kW m^{-2}.

The dependencies of the mean bubble departure diameter $\bar{d}_{\mathrm{b}}$ and mean bubble departure frequency $\bar{f}_{\mathrm{b}}$ versus heat flux at P = 0.1013 MPa are shown in Fig. 9a, b. The mean velocity of bubble growth $\bar{w}_{\mathrm{b}} = \bar{d}_{\mathrm{b}} \cdot \bar{f}_{\mathrm{b}}$ is shown in Fig. 9c.

The obtained results indicate that the bubble departure diameter, frequency and mean velocity of bubble growth are insignificantly changed in the range of studied heat fluxes. Weak change of the bubble departure diameter and frequency, as well as no change of mean velocity of the bubble growth versus heat flux, was reported in [10, 23–26].

The data on the IBC obtained for the R141b at the heat flux 29.6 kW m^{-2} slightly differ from the trends obtained for R141b/Span80 and R141b/Span80/TiO$_2$. That can be gathered with not fully developed boiling process of R141b on Ni–Cr wire at 29.6 kW m^{-2}. For this reason, we do not consider the IBC values for the pure R141b at the heat flux 29.6 kW m^{-2} during modeling.

Modeling section

RPI model performance for the case when the experimental data on nucleation sites density is unavailable

The experimental data on the thermophysical properties for the pure R141b, R141b/Span 80 and R141b/Span 80/TiO$_2$ solutions were reported previously in [27]. It was shown
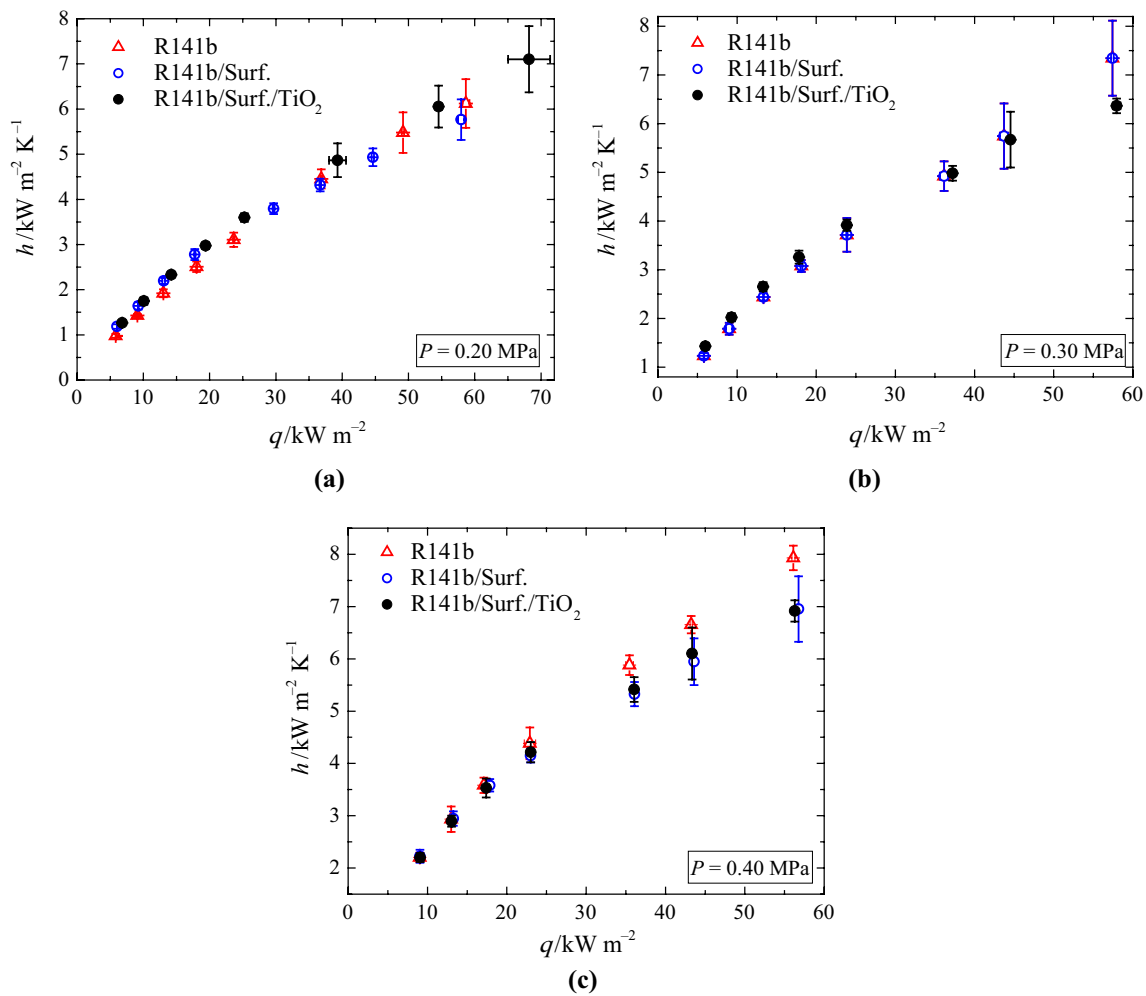
Fig. 6 Pool boiling HTC versus heat flux: **a** 0.2 MPa, **b** 0.3 MPa and **c** 0.4 MPa

Table 2 Coefficients of Eq. (4)

Fluid	0.20 MPa			0.30 MPa			0.40 MPa		
	A	B	RMSE/W m^{-2} K^{-1}	A	B	RMSE/W m^{-2} K^{-1}	A	B	RMSE/W m^{-2} K^{-1}
R141b	1.1732	0.781756	66.6	1.9631	0.748324	95.5	4.3676	0.686787	52.7
R141b/Surf.	3.6585	0.673049	75.5	6.7067	0.627153	126.0	10.3692	0.594978	61.2
R141b/Surf./TiO$_2$	2.4160	0.718459	68.7	4.8583	0.660957	154.5	9.5380	0.603588	93.9

that the effects of the Span 80 (0.10 mass%) and Span 80/TiO$_2$ (0.10/0.10 mass%) admixtures on the density, viscosity, thermal conductivity and surface tension of R141b are insignificant. Therefore, it cannot be assumed as the influencing factor on the HTC [12]. Thus, for the simplicity, in

all calculations presented here, the properties for the pure R141b were taken from the database REFPROP [28].

The RPI model uses the heat flux division scheme for the boiling process and then was adapted for the pool boiling as was shown in [12, 29]. The model considers the following
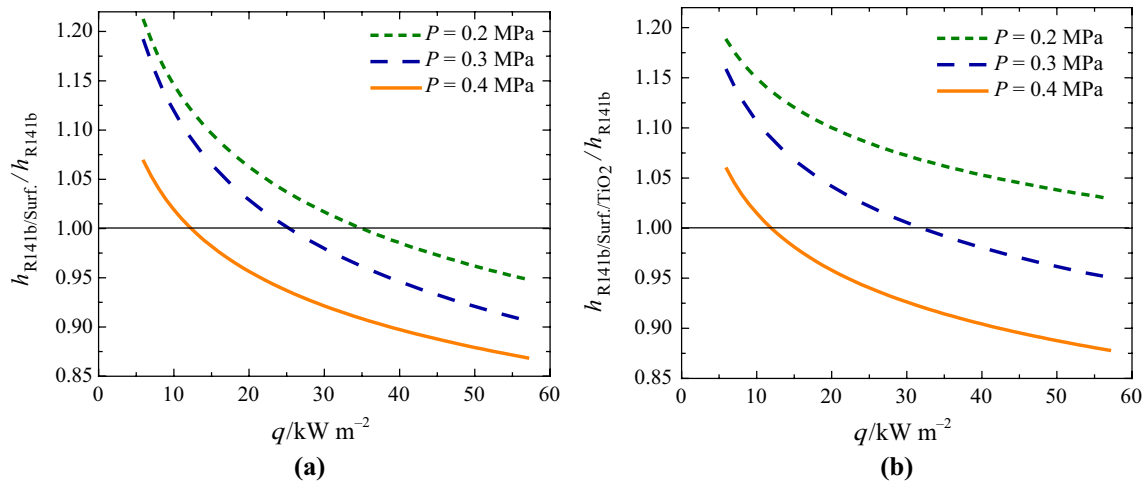
Fig. 7 Relative deviations of the HTC between: **a** pure R141b and R141b/Span 80, **b** pure R141b and R141b/Span 80/TiO₂
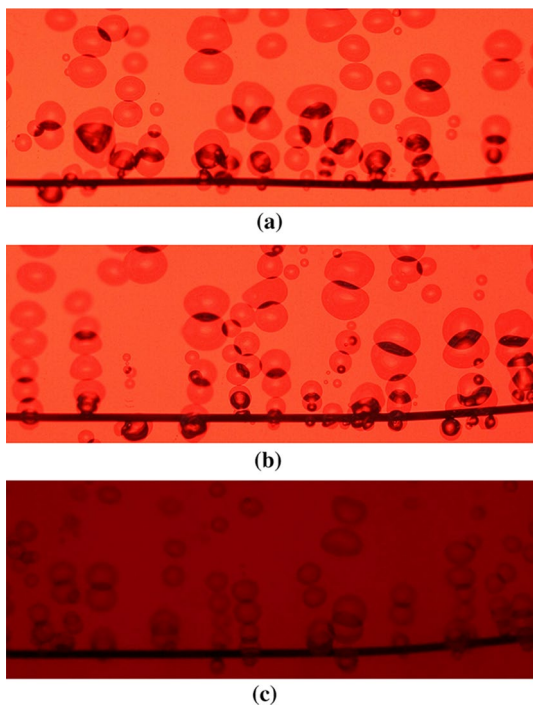

Fig. 8 Snapshots of the pool boiling process for: **a** R141b, **b** R141b/Surf. and **c** R141b/Surf./TiO₂

heat transfer mechanisms: the latent heat of evaporation to form the bubble q_e; heat for reformation of the thermal boundary layer following bubble departure (quenching heat flux) q_q; heat transfer to the liquid by convection in the area outside the influence of bubbles q_c. Thus, the total heat flux q_{tot} during boiling can be calculated as

$$q_{tot} = q_e + q_q + q_c \tag{5}$$

Each of the components of q_{tot} was described in details for pool boiling case in [12, 13]. Depending on the shape and orientation of the heating surface, the convective HTC has to be calculated using corresponding equation. In our case, the formula for a horizontal cylinder was applied [30]

$$h_{conv} = \frac{k}{d_h} 0.5 (\text{Gr} \cdot \text{Pr})^{0.25} \left(\frac{\text{Pr}}{\text{Pr}_w} \right)^{0.25} \tag{6}$$

where Gr and Pr are Grashof and Prandtl numbers, respectively; Pr_w is Prandtl number calculated at the temperature of heating surface.

The model was fed by the experimental data on the mean bubble departure diameter and frequency (see Fig. 9). Two correlations give the dependence of the mean bubble departure diameter [10, 23] and frequency [10] versus pressure

$$\bar{d}_b = \bar{d}_{b\,0.1} \left(\frac{\sigma (\rho'_{0.1} - \rho''_{0.1})}{\sigma_{0.1} (\rho' - \rho'')} \right)^{0.5} \tag{7}$$

$$\bar{w}_b / \bar{w}_{b\,0.1} = \left(\rho''_{0.1} / \rho'' \right)^{2.3 + 0.5 \lg \pi} \tag{8}$$

where $\bar{d}_b$, ρ', ρ'' and σ are the average bubble departure diameter, the density of the liquid and vapor and the surface tension at given pressure; $\bar{d}_{b\,0.1}$, $\rho'_{0.1}$, $\rho''_{0.1}$ and $\sigma_{0.1}$ are the average bubble departure diameter, the density of the liquid and vapor and the surface tension at $P_{0.1} = 0.1013$ MPa; $\bar{w}_b = \bar{d}_b \cdot \bar{f}_b$ is mean velocity of bubble growth at given pressure; $\bar{w}_{b\,0.1}$ is mean velocity of the bubble growth at $P_{0.1} = 0.1013$ MPa; $\pi = P_{0.1} / P_C$ is the reduced pressure.
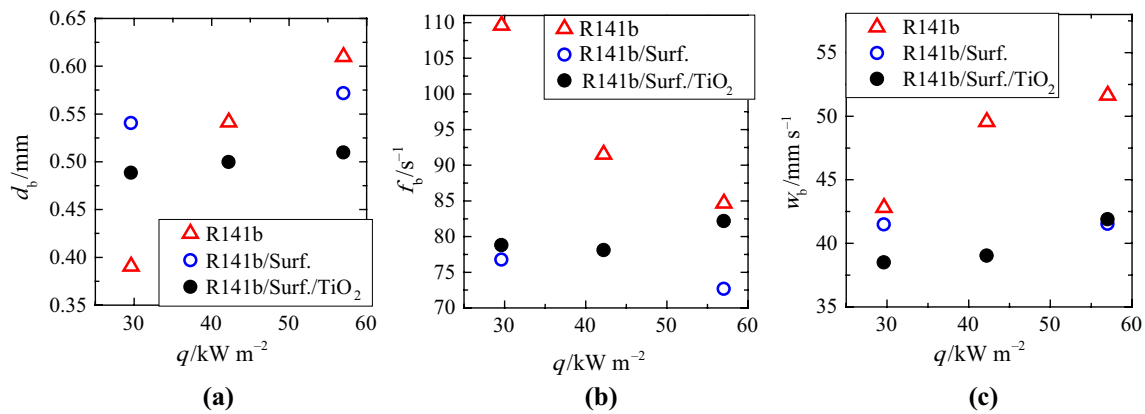
Fig. 9 IBC versus heat flux: **a** bubble departure diameter, **b** bubble departure frequency and **c** mean velocity of bubble growth

The nucleation site density was not measured experimentally and therefore was calculated using the following correlation [10, 23, 31]

$$\sqrt{n_b} = 25 \times 10^{-8} \left(\frac{\Delta h \cdot \rho'' \cdot \Delta T}{T_S \cdot \sigma} \right)^{1.5} \quad (9)$$

where n_b is the nucleation site density, (m⁻²) Δh is the heat of vaporization, (J kg⁻¹); ρ'' is the density of vapor, (kg m⁻³); ΔT is the wall superheat, (K); T_S is the saturation temperature, (K); σ is the surface tension, (N m⁻¹).

The results of RPI model performance to predict the HTC for the case when the experimental data on nucleation sites density are unavailable and Eq. (9) was used to calculate it are shown in Fig. 10. Relative deviations between calculated and experimental data are shown in Fig. 11.

As can be seen, the experimental and calculated values for the HTC are quite close to each other. Relative deviations between them do not exceed ± 20%. However, there is no qualitative agreement between prediction and experiment regarding the effects of the surfactant and nanoparticles. Such results demonstrate high importance of the nucleation site density in the nucleate boiling process.

It is well known that nanoparticles and surfactants may cause the reduction or increase in the nucleation site density [32–35]. This process is influenced by many factors such as boiling regime, boiling pressure/temperature, nanoparticles size and initial roughness of the surface [33]. Such a diversity of influencing parameters on the nucleation site density may explain the controversial results regarding the effects of nanoparticles on the HTC during boiling.

Thus, we can conclude that both qualitatively and quantitatively accurate modeling of the HTC is only possible when the full set of the IBC is considered.

Introducing the limited set of experimental data to improve the HTC prediction

As the following step to increase the accuracy of the HTC prediction, we introduce the limited set of experimental data (LSED) to the calculation process aiming to reduce its amount to the minimum. Firstly, using the experimental data on the HTC, bubble departure diameter and frequency (all in the narrow range of heat flux 25–30 kW m⁻²) the dependencies of the nucleation site density versus heat flux and pressure were calculated for each studied fluid. This approach was previously used and described elsewhere [13]. The transition from atmospheric pressure to the pressures studied in the HTC experiment for the bubble departure diameter and frequency was performed using Eqs. (7–8).

The obtained data on the nucleate site density in range of the heat fluxes 25–30 kW m⁻² were fitted then using Eq. (10). Equation (10) was chosen after analysis of obtained in the study dependences $n_b = f(q)$ in the range of heat fluxes 5.8–56.4 kW m⁻² and at various boiling pressures (0.2, 0.3, 0.4 MPa) for all the studied here liquids.

$$n_b = A \cdot q^B, \quad (10)$$

where A and B are the coefficients.

The analysis of Eq. (9) and dependence $n_b = f(q)$ (calculated with help of the RPI model) have revealed that the nucleation sites density versus pressure for all the studied here liquids follow the correlation

$$n_b = n_{b\,0.1} \left(\frac{\Delta h \cdot \rho''}{T_S \cdot \sigma} \cdot \frac{T_{S\,0.1} \cdot \sigma_{0.1}}{\Delta h_{0.1} \cdot \rho''_{0.1}} \right)^C, \quad (11)$$
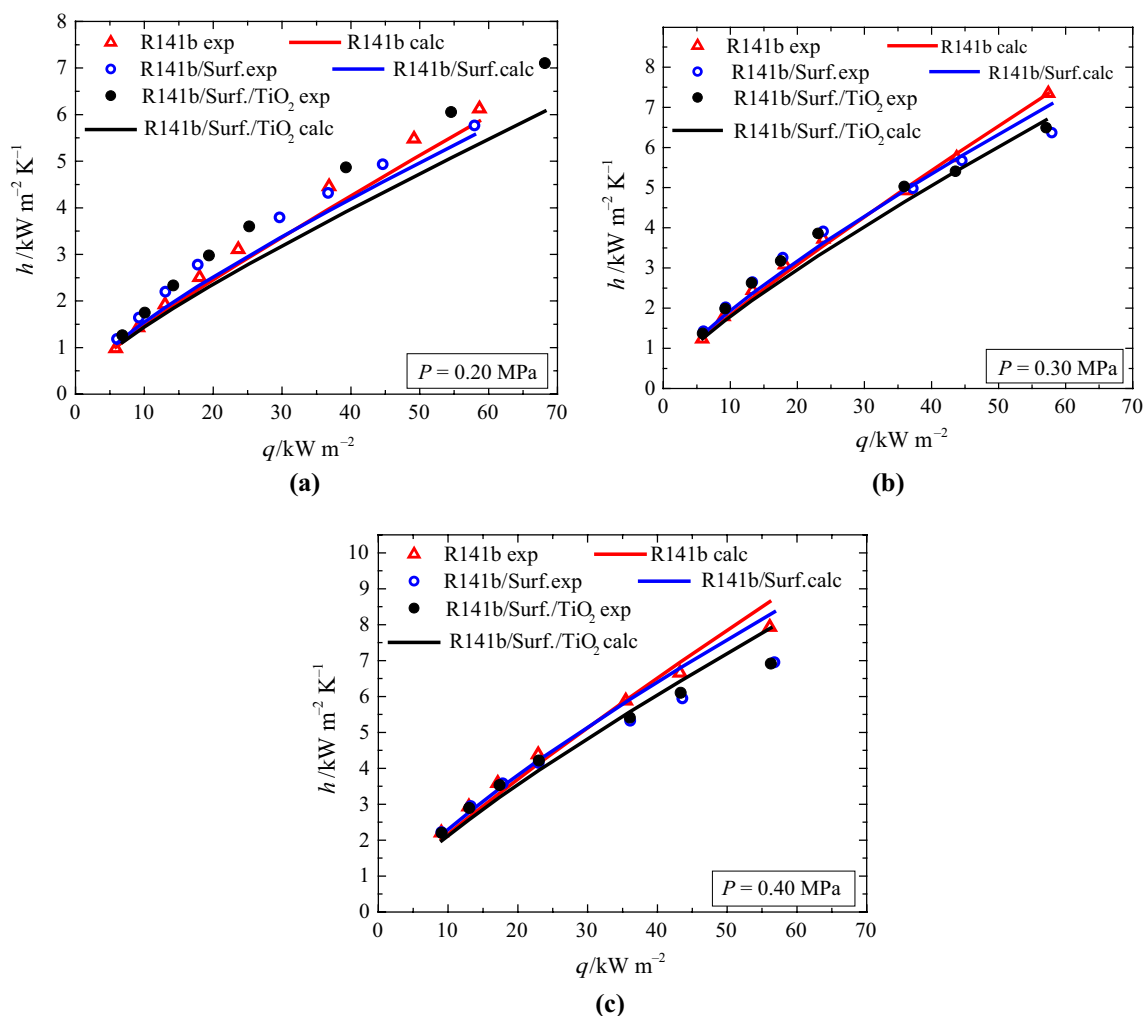
Fig. 10 Comparison of the experimental data for HTC and calculated values by RPI model with calculated n_b for the pure R141b, R141b/Surf. and R141b/Surf./TiO$_2$: **a** 0.2 MPa, **b** 0.3 MPa and **c** 0.4 MPa

where n_b, Δh, ρ'', T_S and σ are the nucleation site density, heat of vaporization, vapor density, saturation temperature and surface tension at given pressure at which the value n_b has to be defined, respectively; $n_{b\,0.1}$, $\Delta h_{0.1}$, $\rho''_{0.1}$, $T_{S\,0.1}$ and $\sigma_{0.1}$ are the same parameters at $P_{0.1} = 0.1013$ MPa, respectively; C is empirical constant. The coefficients of Eqs. (10–11) for each studied liquid are shown in Table 3.

According to [10], the value of C should be similar for different liquids. However, we got quite high difference of C for each tested liquid—see Table 3. Nonetheless, the coefficient C could be found for each specific liquid/surface combination using LSED at one value of the heat flux and two values of pressure. Figure 12 shows the comparison of two calculation methods for the nucleation size density versus heat flux and pressure: (1) using the RPI model according to Eqs. (5, 7–8) and LSED on the HTC, the average values of the bubble departure diameter and frequency and (2) using Eq. (11) and LSED at one value of the heat flux and two values of pressure. As can be seen, both calculations are very similar. Thus, data on the IBC obtained in the narrow range of the heat flux and pressure can be extrapolated for a wide range of the experimental parameters using Eq. 11 [10, 23].

Finally, we have compared the relative deviations of the HTC calculated using LSED within the framework of the RPI model and fitted experimental data by Eq. (4). As follows from Fig. 13, both qualitative and quantitative accuracy of the HTC prediction is achieved when LSED was applied. A visual summary of the proposed method is represented in a form of the scheme in Fig. 14.
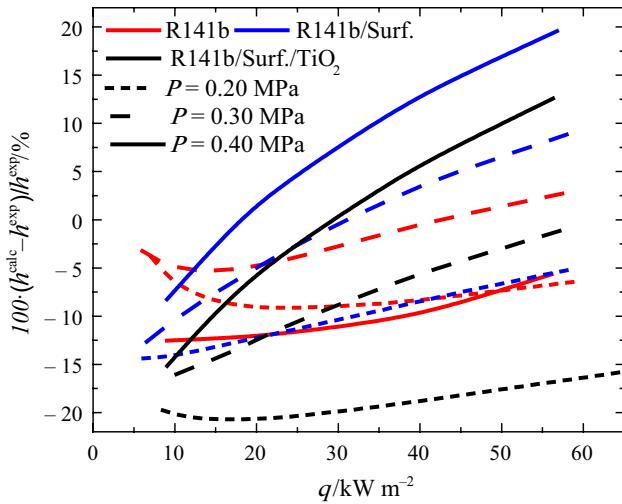
Fig. 11 Relative deviations of the experimental data for HTC and calculated values by RPI model with calculated n_b for the pure R141b, R141b/Surf. and R141b/Surf./TiO$_2$

Table 3 Coefficients of Eqs. (10) and (11)

Fluid	A	B	C
R141b	3748	0.5826	1.20
R141b/Surf.	1007	0.7122	1.09
R141b/Surf./TiO$_2$	2076	0.6682	1.05
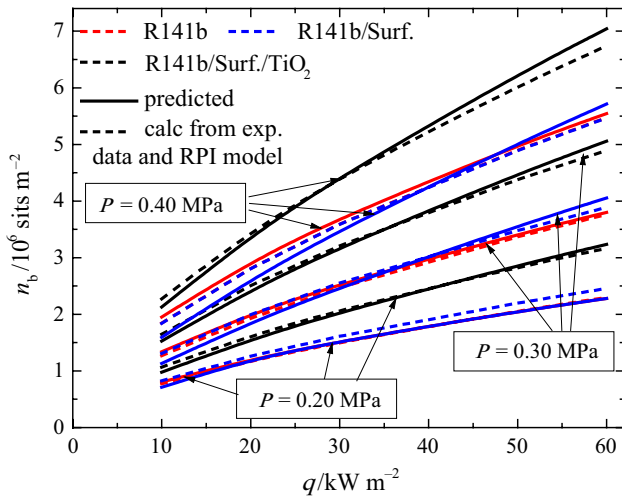
Fig. 12 Nucleation site density versus heat flux density: (solid line) Eq. (11) used together with coefficient C found using LSED at one value of heat flux density (25 kW m^{-2}) and two values of pressure (0.2 and 0.3 MPa); (dashed line) RPI model used together with LSED on the HTC and IBC in the range of heat flux density 25–30 kW m^{-2}
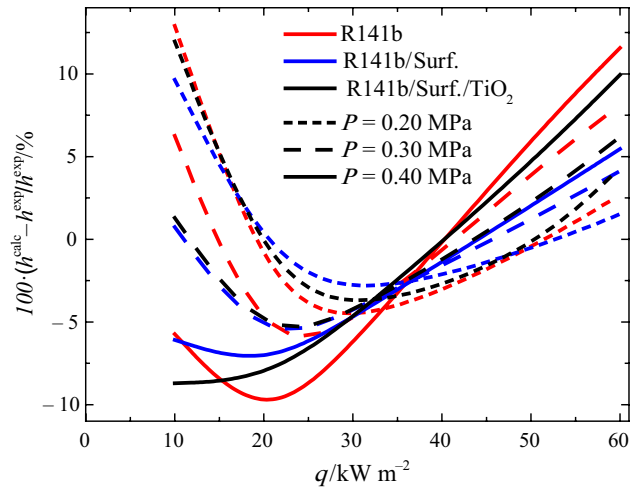

Fig. 13 Relative deviation of the HTC calculated using LSED within framework of the RPI model and fitted experimental data by Eq. (4)
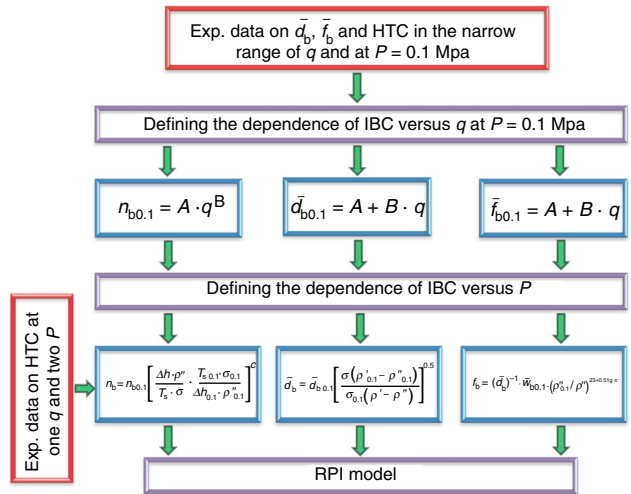

Fig. 14 Scheme of the proposed approach utilizing LSED within the framework of the RPI model

In order to confirm the reliability of the proposed approach, we have examined experimental data for the HTC and IBC reported in [25]. In this work, the nucleate pool boiling experiments of methane were performed in the range of the heat flux from 10 to 80 kW m^{-2} and at the pressures 0.15, 0.20, 0.30 and 0.40 MPa. The experiments were conducted on the upper surface of a smooth vertical copper cylinder. Thereafter, to calculate the HTC under natural convection as part of q_c and q_{tot} Eq. (5) a respective correlation was used [31]. During calculations, all thermophysical properties
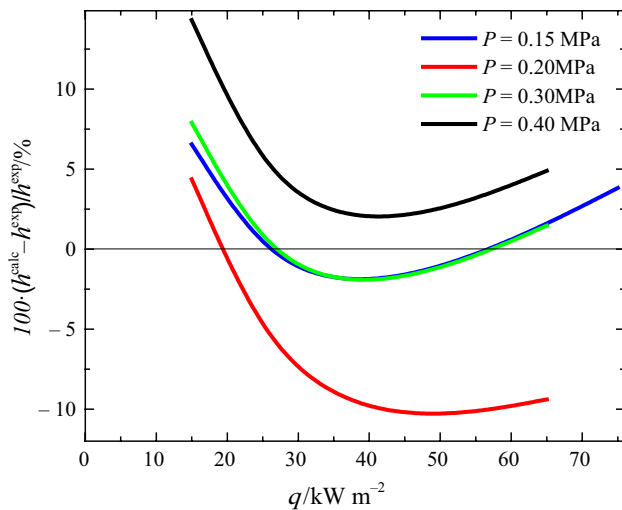
Fig. 15 Relative deviations between experimental [25] and calculated data on the HTC during pool boiling of methane at the flat copper surface

were taken from [28]. The coefficient C of Eq. (11) was found to be equal to 1.39 for this case. The performance of the method is shown in Fig. 15. As can be seen, the relative deviations between experimental [25] and calculated data on the HTC are mainly estimated within $\pm 10\%$.

Conclusions

In this paper, the experimental data on the HTC and IBC were obtained for pure refrigerant R141b and its mixtures with surfactant Span 80 and TiO$_2$ nanoparticles. The results indicate that the increase in the HTC is higher at the lower heat flux and pressure. The increase in the heat flux and pressure mitigates the effect of the surfactant and nanoparticles on the HTC and leads to decrease in the HTC comparing to the pure refrigerant. The obtained results on the IBC show that the bubble departure diameter, frequency and mean velocity of the bubble growth are insignificantly change in the range of the examined heat flux.

The analysis of the RPI model performance for the case when experimental data on the nucleation sites density is unavailable was carried out. It was shown that no qualitative agreement exists between experimental and calculated data on the HTC. In order to improve the accuracy of the HTC prediction during the pool boiling, we proposed a new approach that combines a limited set of the experimental data (LSED) with correlations of the IBC's versus heat flux and pressure. More specifically, LSED included the average bubble departure diameter and frequency measured at one pressure and two values of the heat flux, as well as the HTC

determined at one value of the heat flux and two values of pressure.

As the result, the LSED makes it possible to achieve both qualitative and quantitative (within $\pm 10\%$) agreement between predicted and experimental data on the pool boiling HTC obtained here for the R141b, R141b/Span 80 and R141b/Span 80/TiO$_2$ and reported data for methane [25].

References

1. Thome JR. Engineering data book III. Huntsville: Wolverine Tube Inc; 2004.
2. Mostinski IL. Application of the rule of corresponding states for calculation of heat transfer and critical heat flux. Teploenergetika. 1963;4:66–71.
3. Cooper MG. Heat flow rates in saturated nucleate pool boiling-a wide-ranging examination using reduced properties. Adv Heat Transf. 1984;16:157–239. https://doi.org/10.1016/S0065-2717(08)70205-3.
4. Stephan P, Kabelac S, Kind M, Martin H, Mewes D, Schaber K. VDI heat atlas. Springer; 2010. https://doi.org/10.1007/978-3-540-77877-6.
5. Ribatski G, Jabardo JMS. Nucleate boiling of halocarbon refrigerants: heat transfer correlations. HVAC&R Res. 2000;6:349–67. https://doi.org/10.1080/10789669.2000.10391421.
6. Rohsenow WM. A method of correlating heat transfer data for surface boiling of liquids. Cambridge: MIT Division of Industrial Cooporation; 1951.
7. Kutateladze SS. Heat transfer and hydrodynamic resistance: handbook. chap. 12.7. Moscow: Energoatomizdat; 1990 **(in Russian)**.
8. Jung D, Kim Y, Ko Y, Song K. Nucleate boiling heat transfer coefficients of pure halogenated refrigerants. Int J Refrig. 2003;26:240–8. https://doi.org/10.1016/S0140-7007(02)00040-3.
9. Stephan K, Abdelsalam M. Heat-transfer correlations for natural convection boiling. Int J Heat Mass Transf. 1980;23:73–87. https://doi.org/10.1016/0017-9310(80)90140-4.
10. Tolubinsky VI. Heat transfer at boiling. Kyiv: Kyiv Nauk Dumka; 1980 **(in Russian)**.
11. Kurul N, Podowski MZ. Multidimensional effects in forced convection subcooled boiling. In: International Heat Transfer Conference Digital Library, Begel House Inc.; 1990.
12. Gerardi C, Buongiorno J, Hu L, McKrell T. Study of bubble growth in water pool boiling through synchronized, infrared thermometry and high-speed video. Int J Heat Mass Transf. 2010;53:4185–92. https://doi.org/10.1016/j.ijheatmasstransfer.2010.05.041.
13. Nikulin A, Khliyeva O, Lukianov N, Zhelezny V, Semenyuk Y. Study of pool boiling process for the refrigerant R11, isopropanol and isopropanol/Al$_2$O$_3$ nanofluid. Int J Heat Mass Transf. 2018;118:746–57. https://doi.org/10.1016/j.ijheatmasstransfer.2017.11.008.
14. Trisaksri V, Wongwises S. Nucleate pool boiling heat transfer of TiO$_2$–R141b nanofluids. Int J Heat Mass Transf. 2009;52:1582–8. https://doi.org/10.1016/j.ijheatmasstransfer.2008.07.041.

15. Kourti T. Turbidimetry in particle size. Analysis. 2000. https://doi.org/10.1002/9780470027318.a1517.
16. Crawley G, Cournil M, Di Benedetto D. Size analysis of fine particle suspensions by spectral turbidimetry: potential and limits. Powder Technol. 1997;91:197–208. https://doi.org/10.1016/S0032-5910(96)03252-4.
17. Zhelezny VP, Lukianov NN, Khliyeva OY, Nikulina AS, Melnyk AV. A complex investigation of the nanofluids R600a-mineral oil-Al$_2$O$_3$ and R600a-mineral oil-TiO$_2$. Thermophysical properties. Int J Refrig. 2017;74:488–504. https://doi.org/10.1016/j.ijrefrig.2016.11.008.
18. Nikulin A, Moita AS, Moreira ALN, Murshed SMS, Huminic A, Grosu Y, et al. Effect of Al$_2$O$_3$ nanoparticles on laminar, transient and turbulent flow of isopropyl alcohol. Int J Heat Mass Transf. 2019;130:1032–44. https://doi.org/10.1016/J.IJHEATMASSTRANSFER.2018.10.114.
19. Nikulin A, Khliyeva O, Zhelezny V, Semenyuk Y, Lukianov N, Moreira ALN. How does change of the bulk concentration affect the pool boiling of the refrigerant oil solutions and their mixtures with surfactant and nanoparticles? Int J Heat Mass Transf. 2019;137:868–75. https://doi.org/10.1016/J.IJHEATMASSTRANSFER.2019.03.109.
20. Taylor BN, Kuyatt C. Guidelines for evaluating and expressing the uncertainty of NIST measurement results 1994 Edition. 1994.
21. Peng H, Ding G, Hu H. Effect of surfactant additives on nucleate pool boiling heat transfer of refrigerant-based nanofluid. Exp Therm Fluid Sci. 2011;35:960–70. https://doi.org/10.1016/J.EXPTHERMFLUSCI.2011.01.016.
22. Cheng L, Mewes D, Luke A. Boiling phenomena with surfactants and polymeric additives: a state-of-the-art review. Int J Heat Mass Transf. 2007;50:2744–71. https://doi.org/10.1016/j.ijheatmasstransfer.2006.11.016.
23. Pioro IL, Rohsenow W, Doerffer SS. Nucleate pool-boiling heat transfer. I: Review of parametric effects of boiling surface. Int J Heat Mass Transf. 2004;47:5033–44. https://doi.org/10.1016/j.ijheatmasstransfer.2004.06.019.
24. Sharma PR, Lee A, Harrison T, Martin E, Neighbors K. Effect of pressure and heat flux on bubble departure diameters and bubble emission frequency. Grambling: Grambling State University; 1996.
25. Chen H, Chen G, Zou X, Yao Y, Gong M. Experimental investigations on bubble departure diameter and frequency of methane saturated nucleate pool boiling at four different pressures. Int J Heat Mass Transf. 2017;112:662–75. https://doi.org/10.1016/J.IJHEATMASSTRANSFER.2017.05.031.
26. McHale JP, Garimella SV. Bubble nucleation characteristics in pool boiling of a wetting liquid on smooth and rough surfaces. Int J Multiph Flow. 2010;36:249–60. https://doi.org/10.1016/J.IJMULTIPHASEFLOW.2009.12.004.
27. Khliyeva O, Lukianova T, Semenyuk Y, Zhelezny V. Experimental study of the effect of TiO$_2$ nanoparticles on the thermophysical properties of the R141b refrigerant. Eastern-Eur J Enterp Technol. 2018;6:33–42. https://doi.org/10.15587/1729-4061.2018.147960.
28. Lemmon EW, Huber ML, McLinden MO. NIST reference fluid thermodynamic and transport properties–REFPROP. NIST Stand Ref Database. 2002;23:v7.
29. Gerardi C, Buongiorno J, Hu L, McKrell T. Infrared thermometry study of nanofluid pool boiling phenomena. Nanoscale Res Lett. 2011;6:232. https://doi.org/10.1186/1556-276X-6-232.
30. Isachenko V, Osipova V, Sukomel A. Teploperedacha (Heat transfer). Moscow: Energomash; 1981 **(in Russian)**.
31. Zhokhov KA. Number of vapour generating centers. In: Aerodynamics heat transfer work element power equipment. Leningrad, Russ 1969:131–5.
32. Liang G, Mudawar I. Review of pool boiling enhancement with additives and nanofluids. Int J Heat Mass Transf. 2018;124:423–53. https://doi.org/10.1016/J.IJHEATMASSTRANSFER.2018.03.046.
33. Liang G, Mudawar I. Review of pool boiling enhancement by surface modification. Int J Heat Mass Transf. 2019;128:892–933. https://doi.org/10.1016/J.IJHEATMASSTRANSFER.2018.09.026.
34. Ciloglu D, Bolukbasi A. A comprehensive review on pool boiling of nanofluids. Appl Therm Eng. 2015;84:45–63. https://doi.org/10.1016/J.APPLTHERMALENG.2015.03.063.
35. Kiyomura IS, Manetti LL, da Cunha AP, Ribatski G, Cardoso EM. An analysis of the effects of nanoparticles deposition on characteristics of the heating surface and ON pool boiling of water. Int J Heat Mass Transf. 2017;106:666–74. https://doi.org/10.1016/J.IJHEATMASSTRANSFER.2016.09.051.